JOURNAL OF THERMOPHYSICS AND HEAT TRANSFER
Vol. 12, No. 3, July–September 1998

Modeling Cyclic Phase Change and Energy Storage in Solar Heat Receivers

Carsie A. Hall III,* Emmanuel K. Glakpe,† and Joseph N. Cannon‡
Howard University, Washington, D.C. 20059
and
Thomas W. Kerslake§
NASA Lewis Research Center, Cleveland, Ohio 44135

Numerical results pertaining to cyclic melting and freezing of an encapsulated phase-change material (PCM), integrated into a solar heat receiver, have been reported. The cyclic nature of the present problem is relevant to latent heat thermal energy storage systems used to power solar Brayton engines in space. Specifically, a physical and numerical model of the solar heat receiver component of NASA Lewis Research Center's ground test demonstration (GTD) system was developed and results compared with available experimental data. Multiconjugate effects such as the convective flow of a low Prandtl number fluid, conduction in the PCM, containment tube, and working fluid conduit were accounted for in the model. An ideal-body thermal radiation model was also included to quantify reradiative effects inside the receiver along with losses through the aperture and receiver shell. A high-temperature eutectic mixture of $\mathrm{LiF{-}CaF_2}$ was used as the PCM and a mixture of He/Xe was used as the working fluid. A modified version of the computer code HOTTube was used to generate results for comparisons with GTD experimental data in both subcooled and two-phase regimes. While qualitative trends were in close agreement for the balanced-orbit modes, excellent quantitative agreement was observed for steady-state modes.

Nomenclature

A = metal and PCM cross-sectional area
c = specific heat of metal and PCM
c_p = working fluid specific heat at constant pressure
f = geometric view factor
h = enthalpy per unit mass
h^* = convective heat transfer coefficient
h_{sf} = PCM latent heat of fusion
L = active tube or cavity length
M = total number of axial nodes along tube
$\dot{m}$ = working fluid mass flow rate
N = total number of tubes in receiver
$\mathbf{n}$ = outer unit normal
P = wetted perimeter
$\dot{Q}$ = heat transfer rate
$\dot{q}''$ = heat transfer rate per unit area
R = thermal resistance of metal and PCM
r = radial coordinate
S^* = geometric shape factor for finned tube
T, T_m = temperature, PCM phase-transition temperature
t = time
$\mathbf{U}$ = velocity vector
W = thickness of a single PCM canister
X = PCM liquid fraction
z = axial coordinate
θ = dimensionless working fluid temperature
κ = shell loss function
ρ = density
σ = Stefan–Boltzmann constant
ω = turboalternator compressor speed

Subscripts

abs = absorbed
ap = aperture
av = average
cav = receiver cavity
ch = finned-tube fluid channel
f = working fluid
in = working fluid inlet
l = liquid PCM
max = maximum
out = working fluid outlet
ref = reference value
s = solid PCM
shell = outer cavity region

Superscripts

n = previous time level
$n + 1$ = current time level

Introduction

THE intermittent nature of solar energy availability for low-earth orbit (LEO) applications presents a particular challenge for space-power management schemes during traversal of spacecraft or satellites into Earth's shadow (eclipse phase). One alternative to photovoltaics (PV) with battery storage is solar dynamics with latent heat thermal energy storage (LHTES) via solar heat receivers. Solar heat receivers are very instrumental components in the production of electric power using solar dynamic power (SDP) systems. In a typical operation, the SDP system uses 1) a concentrator to collect and focus the incident energy onto the aperture plane of a central receiver; 2) a central receiver to collect and distribute, with minimal losses, the reflected energy from the concentrator; 3)

Presented as Paper 97-2452 at the AIAA 32nd Thermophysics Conference, Atlanta, GA, June 23–25, 1997; received July 14, 1997; revision received Oct. 31, 1997; accepted for publication Dec. 19, 1997.

*Research Associate, College of Engineering, Architecture and Computer Sciences, Department of Mechanical Engineering. Student Member AIAA.

†Professor, College of Engineering, Architecture and Computer Sciences, Department of Mechanical Engineering. Member AIAA.

‡Professor, College of Engineering, Architecture and Computer Sciences, Department of Chemical Engineering.

§Power Systems Engineer, Power and Propulsion Office, Analysis and Management Branch.

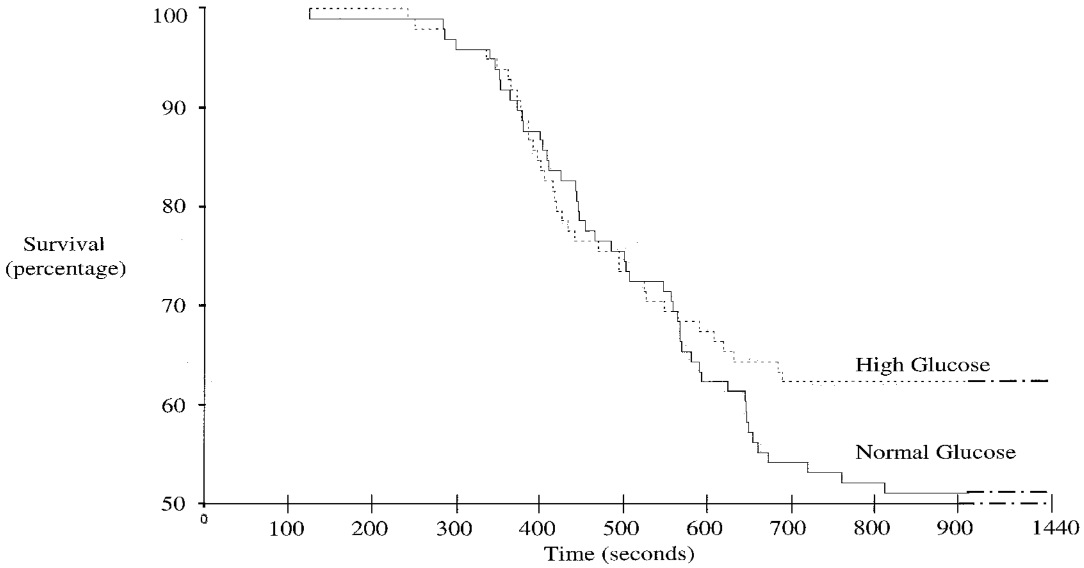

Fig. 1 Thermodynamic cycle for closed Brayton engine integrated with solar heat receiver.

working fluid tubes aligned along the periphery of the receiver to absorb the distributed energy as heat, thus, raising the temperature of the working fluid (typically a low-Prandtl-number fluid) flowing through the tubes; 4) a turbine to expand the high-temperature working fluid to produce mechanical work via a rotating shaft; 5) a compressor to circulate the working fluid through the working fluid tubes; and 6) an alternator to convert mechanical shaft motion into electric power. A recuperator is added to increase the thermal efficiency of the thermodynamic cycle (typically a closed Brayton cycle as depicted in Fig. 1).

Solar heat receivers employing encapsulated phase-change materials (PCMs) have the advantage over sensible heat receivers of requiring less mass while possessing higher energy storage densities. This, in turn, makes them ideal candidates for energy storage in the space environment where temperatures are sufficiently high and PCMs with high latent heats of fusion become indispensable. In this regard, phase-change salts such as the eutectic mixture LiF–CaF_2, which has a melting point of 1413°F (767°C) and a heat of fusion of 340 Btu/lbm (789 kJ/kg), lend themselves as favorable candidates for LHTES in the harsh space environment.

Investigations on modeling and testing solar heat receivers and/or their subcomponents employing phase-change storage have appeared in the literature. Strumpf and Coombs[1] conducted an experimental investigation to quantify the thermal performance of the receiver tube section of a solar heat receiver subject to a simulated solar flux (using a heater panel with heater wires embedded in an insulating material), cycled to approximate orbital conditions using air as the Brayton engine working fluid. Sedgwick[2] employed two receiver thermal models that used an implicit finite difference scheme to solve the resulting energy equations. The first model assumed a fixed melt temperature and explicitly tracked the location of the phase (solid/liquid) front. The second algorithm modeled the latent energy storage as an equivalent sensible energy storage over a small but finite temperature range while updating nodal conductances and thermal capacitances. The computer code RADSIM (radiation simulation) was used to calculate solar flux distributions, cavity geometric view factors, and, ultimately, radiation (two-band) heat losses. In the work of Wichner et al.,[3] a finite difference scheme was used for the thermal analysis while a finite element scheme was used for the stress analysis of a single canister model. The effects of solidification front behavior were simulated to include conduction in the solid/liquid phases and canister material, void growth/shrinkage, radiation heat transfer across the void, and convection in the melt from either the Marangoni effect (in reduced gravity, $\approx 10^{-4}$ g) or buoyancy effects in 1-g environments. A three-dimensional model (computer code NORVEX) was formulated by Wilson and Flanery[4] to analyze the cyclic melting and freezing, fluid flow, and void formation and movement in a hollow metal canister filled with a high-temperature PCM.

Kerslake and Ibrahim[5] developed a two-dimensional, axisymmetric finite difference model of a Space Station *Freedom* thermal energy storage canister. A eutectic mixture of LiF–CaF_2 was used as the latent energy storage PCM and the superalloy Haynes 188 was used as its containment material. In their model, the effects of conduction in the canister walls and PCM solid, conduction, and free convection in the liquid PCM, and conduction and radiation across a stationary void region, i.e., no volume change effects, filled with low vapor pressure PCM were evaluated. The void was placed adjacent to the canister outer wall.

Drake[6] developed a three-dimensional model of a PCM canister (LiF PCM with superalloy Haynes 188 containment material) undergoing cyclic melt/freeze cycles with void movement and Marangoni flow effects. The discretized equations were solved via the semi-implicit Crank–Nicholson scheme using a Newton method with Cholesky factorization. The mushy zone was treated as a porous medium and the volume of fluid (VOF) method of Hirt and Nichols[7] was used to track the void, which was treated as a compressible fluid with zero viscosity. Kerslake[8] used the computer program NUCAM-2DV to model a two-dimensional, axisymmetric canister using an explicit finite difference technique. The enthalpy method was employed, and a fixed location, constant void volume with conduction and radiation was modeled. The working fluid used in this model was air.

Strumpf et al.[9,10] modeled a solar heat receiver using the computer code SOLREC-TSD (solar receiver–thermal storage device), a three-dimensional, transient, finite element code. This code contained three modules: 1) a cavity radiation network solver, 2) a detailed finite element receiver thermal storage model, and 3) a transient heat exchanger fluid solver. Only one-half of the canister was modeled because of imposed symmetry conditions. Sedgwick[11] reported on the first-ever full-size solar dynamic heat receiver, with a thermal output of 102 kW. The receiver was designed to the specifications of the Space Station *Freedom* SDP system. It was tested in a vacuum chamber with liquid nitrogen cooling shrouds and an aperture cold plate to partially simulate the LEO vacuum environment. Scarda[12] modeled the NASA Lewis Research Center's TES-1 experiment using a two-dimensional SINDA85 model. The

TES-1 experiment consisted of a torus-shaped canister, conductor rod, and radiator flare. A heater was used to radiate heat to the outer radius of the canister during the melt cycle. After the PCM (LiF) completely melted, the heater was turned off and the stored latent heat was transferred to the conductor rod where it was eventually radiated to the environment by the TES radiator flare during the freeze cycle. The results of the first flight experiment, the TES experiment, to study melting and freezing under microgravity conditions were reported by Namkoong et al.[13] One of the experiments, TES-1, which used LiF PCM and superalloy Haynes 188 containment material, was reported to perform flawlessly in its 22 h of operation. PCM melting was induced by thermal radiation from a heater sleeve surrounding the canister and PCM freezing was induced by shutting the power to the heater and opening the shutter, allowing the stored energy to conduct to the central rod and onto a radiator disk to reject the heat to space. In addition, the computer code TESSIM was used to predict the behavior of the PCM in the canister.

Shaltens and Mason[14] reported experimental results on the operational performance of the NASA Lewis Research Center's Solar Dynamic ground test demonstration (GTD) system. Their results are shown for various insolation levels and operating speeds, and in five primary operating modes: 1) orbital startup, 2) transient, 3) balanced-orbit, 4) steady state, and 5) shutdown.

In the present paper, a physical and numerical model is developed to study the cyclic behavior of the solar heat receiver component of the aforementioned GTD system. The numerical results are compared with the experimental results in the balanced-orbit mode and steady-state mode for both the subcooled and two-phase regimes. Results are reported in the form of maximum and average canister outer surface temperatures, receiver gas-exit temperatures, and receiver melt fraction, all as functions of insolation level and operating speed (via an equivalent mass flow rate). Predicting the thermal performance is critical in determining the so-called thermal state-of-charge (SOC) of solar heat receivers as a function of measurable parameters (Jeffries et al.[15] indicated the need for identifying techniques to appropriately quantify the energy state of the receiver via an SOC algorithm through judicious selection of measurable system parameters). Knowledge of the SOC[16] allows for better control strategies relating to power-management schemes during such operations as cold startup, peak power, and emergency shutdowns with subsequent restarts.

Description of the GTD System

The GTD system is the world's first full-scale demonstration of reliable production of electric power via solar dynamics (SD) technology. This government/industry collaboration is carried out in the NASA Lewis Research Center's large thermal/vacuum facility (tank 6). This facility is equipped to provide simulated solar flux in high vacuum, similar to that which is encountered in LEO. The primary objectives of this project are to demonstrate, using flight prototypical components, that system power delivered and system efficiency both fall within the design target. Moreover, most of the hardware used in the GTD system is derived from the SD system designed for Space Station *Freedom*.[15]

The 2-kWe (nominal) GTD system consists of an off-axis solar concentrator and solar heat receiver with LHTES, both of which are integrated with a closed Brayton engine (power conversion unit or PCU). A more complete description of the GTD system can be found in the paper by Shaltens and Mason.[14]

GTD Solar Heat Receiver Modeling

Problem Description

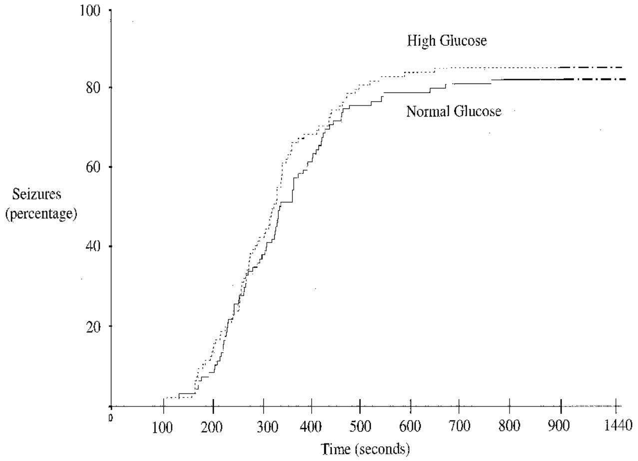

Fig. 2 GTD solar heat receiver (provided by AlliedSignal Aerospace).

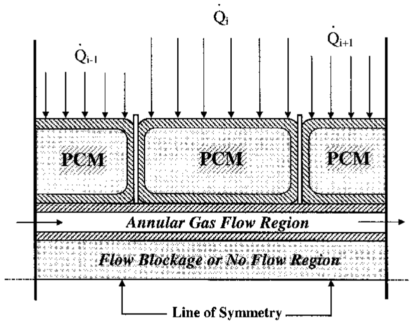

Fig. 3 Schematic of encapsulated PCM tube configuration with annular gas flow.

The physical geometry for the present study is depicted in Fig. 2 and the more detailed single-tube model is shown in Fig. 3. It should be pointed out here that the flow cross section of the working fluid tube is actually finned to augment heat transfer into the working fluid. Furthermore, it is assumed that each tube in the solar receiver is imparted with the same incident solar flux; therefore, only a single tube needs to be analyzed, with a subsequent summation over all tubes to quantify the total receiver thermal performance. Additional assumptions are imposed as follows:

1) No PCM convective motions as a result of buoyancy, the Marangoni effect, or solidification shrinkage/melt expansion.

2) Phase change takes place at a distinct temperature.

3) The PCM is optically opaque.

4) The working fluid flow is hydrodynamically and thermally fully developed.

5) The incident and absorbed solar flux distribution is circumferentially uniform.

GTD Specifications

The specifications for the solar heat receiver of the GTD system used for modeling, in which the present numerical results are reflected, are outlined as follows: 1) effective cavity diameter = 1.56 ft (47.55 cm), 2) aperture diameter = 7 in. (17.78 cm), 3) active tube length = 2 ft (60.96 cm), 4) canister o.d. = 1.78 in. (4.52 cm), 5) hydraulic diameter = 0.045 in. (0.1143 cm), 6) number of tubes in the receiver = 23, 7) number of canisters per tube = 24, 8) canister material = superalloy Haynes 188, 9) PCM = eutectic mixture of LiF–CaF_2 (80.5% LiF by mole), and 10) working fluid = helium/xenon (He/Xe) with a molecular weight of 83.8.

The GTD design is essentially a scaled-down version of the Space Station *Freedom* SDP system that was designed to yield a nominal alternator power output of 35 kWe.

Governing Equations

The generalized integral equation governing the evolution of the enthalpy per unit mass for a region (denoted as k) is given by

$$\frac{\partial}{\partial t}\int_{V_k} \rho_k h_k \, \mathrm{d}V_k = -\int_{S_k} \rho_k h_k \boldsymbol{U}_k \cdot \boldsymbol{n}_k \, \mathrm{d}S_k - \int_{S_k} \boldsymbol{q}'' \cdot \boldsymbol{n}_k \, \mathrm{d}S_k \tag{1}$$

which is coupled to the temperature of the kth region by the equation of state

$$h_k - h_{\mathrm{ref}} = \int_{T_{\mathrm{ref}}}^{T_k} c_k(T_k') \, \mathrm{d}T_k' \tag{2}$$

where each of the k regions is identified as follows: $k = 1$ (outer canister region), $k = 2$ (PCM region), $k = 3$ (inner canister region), $k = 4$ (working fluid tube region), and $k = 5$ (working fluid region). In the solid regions and liquid PCM region, $\boldsymbol{U}_k = \boldsymbol{0}$ (no convective motion). The specific heat c_k in Eq. (2) is assumed to be a linearly increasing function of temperature in the containment canister and working fluid tube regions, but phasewise constant in the PCM region.

Discrete Representations

The containment canister outer and inner regions along with the working fluid tube region are all considered radially lumped. As a result, the radial index j corresponding to the representative temperatures of those regions are $j = 1$, $j = j\mathrm{max}-1$, and $j = j\mathrm{max}$ for the outer canister, inner canister, and working fluid tube regions, respectively. The remaining PCM region is divided into $j\mathrm{max}-3$ nodes, for each ith axial location along the tube.

Applying Eq. (1) to a control volume at the ith outer canister location ($k = 1$) along the tube results in

$$(\rho A)_1 \Delta z \left(\frac{h_{1_{i,j}}^{n+1} - h_{1_{i,j}}^{n}}{\Delta t}\right) = \dot{Q}_{\mathrm{abs}_i}^{n} - \left(\frac{T_{2_{i,j+1}}^{n} - T_{1_{i,j}}^{n}}{R_{1_{i,j+1}}}\right) \tag{3}$$

where i is the discrete index corresponding to the axial direction ($i = 1, 2, \ldots, M$); j is the discrete index corresponding to the radial direction ($j = 1, 2, \ldots, j\mathrm{max}$); n is the discrete index for the previous time level; and $n + 1$ is the discrete index for the current time level. For the PCM region ($k = 2$), the discrete equation is expressed as

$$(\rho A)_2 \left(\frac{h_{2_{i,j}}^{n+1} - h_{2_{i,j}}^{n}}{\Delta t}\right) = \left(\frac{T_{2_{i,j+1}}^{n} - T_{2_{i,j}}^{n}}{R_{2_{i,j+1}}}\right) - \left(\frac{T_{2_{i,j-1}}^{n} - T_{2_{i,j}}^{n}}{R_{2_{i,j-1}}}\right) \tag{4}$$

which is valid in the region $2 \le j \le j\mathrm{max}-2$. Another important consideration is that because the reference level for the PCM enthalpy per unit mass is in the subcooled regime, and is somewhat arbitrary, a flag based on temperature is used to indicate proximity to the melting point. As a result, a similar equation governing the fraction of PCM mass in the liquid phase is given by

$$\frac{m_{i,j} h_{sf}}{W} \left(\frac{X_{i,j}^{n+1} - X_{i,j}^{n}}{\Delta t}\right) = \left(\frac{T_{2_{i,j+1}}^{n} - T_{2_{i,j}}^{n}}{R_{2_{i,j+1}}}\right) - \left(\frac{T_{2_{i,j-1}}^{n} - T_{2_{i,j}}^{n}}{R_{2_{i,j-1}}}\right) \tag{5}$$

where the liquid fraction for the ith axial canister location and jth node is in the range $0 \le X_{i,j} \le 1$. In addition, the specific enthalpy of the PCM shown in Eq. (4) is related to the PCM temperature via an equation of state in accordance with the enthalpy method, i.e.,

$$h - h_{\mathrm{ref}} = c_s(T - T_{\mathrm{ref}}), \qquad T < T_m \tag{5a}$$

in the subcooled regime, and

$$h - h_{\mathrm{ref}} = c_s(T_m - T_{\mathrm{ref}}) + h_{sf} + c_l(T - T_m), \qquad T > T_m \tag{5b}$$

in the superheated regime. Furthermore, the discrete equations governing the evolution of enthalpy per unit mass for the canister inner region ($k = 3$) and working fluid tube region ($k = 4$) are derived as

$$(\rho A)_3 \left(\frac{h_{3_{i,j}}^{n+1} - h_{3_{i,j}}^{n}}{\Delta t}\right) = \left(\frac{T_{4_{i,j+1}}^{n} - T_{3_{i,j}}^{n}}{R_{3_{i,j+1}}}\right) - \left(\frac{T_{2_{i,j-1}}^{n} - T_{3_{i,j}}^{n}}{R_{3_{i,j-1}}}\right) \tag{6}$$

$$(\rho A)_4 \Delta z \left(\frac{h_{4_{i,j}}^{n+1} - h_{4_{i,j}}^{n}}{\Delta t}\right) = \dot{Q}_{f_i}^{n} - \left(\frac{T_{3_{i,j-1}}^{n} - T_{4_{i,j}}^{n}}{R_{4_{i,j-1}}}\right) + \left(\frac{T_{4_{i+1,j}}^{n} - T_{4_{i,j}}^{n}}{R_{4_{i+1,j}}}\right) + \left(\frac{T_{4_{i-1,j}}^{n} - T_{4_{i,j}}^{n}}{R_{4_{i-1,j}}}\right) \tag{7}$$

For the working fluid region ($k = 5$), a one-dimensional, quasi-steady model for the axial transport of enthalpy per unit mass is used. The use of this model is justified by the small hydraulic diameter of the finned-tube working fluid region and low thermal capacitance of the low Prandtl number (for a gas) working fluid. A modified version of the closed-form solution given by (for an isothermal wall condition)

$$\theta(z) = \frac{T_s - T_f}{T_s - T_{\mathrm{in}}} = \exp\left(-\frac{Ph^* z}{\dot{m} c_p}\right) \tag{8}$$

is written for the present configuration as

$$\theta_i^{n+1} = \frac{T_{s_i}^{n+1} - T_{f_i}^{n+1}}{T_{s_i}^{n+1} - T_{\mathrm{in}_i}^{n+1}} = \exp\left(-\frac{P_{\mathrm{ch}} N_{\mathrm{ch}} N S^* h^* \Delta z}{\dot{m} c_p}\right) \tag{9}$$

where P_{ch} is the channel-wetted perimeter, N_{ch} is the number of channels in each finned tube, N is the number of tubes in the receiver, and S^* is a geometric shape factor (estimated to be in the range $0.3 \le S^* \le 1$), used to account for the degree of departure from triangularity of the finned-tube cross section. h^* is obtained from experimental Nusselt number correlations or from analytic theory. Finally, the net rate of axially convected enthalpy, used in Eq. (7), is expressed as

$$\dot{Q}_{f_i}^{n} = \dot{m} c_p (T_{f_{i-1}}^{n} - T_{f_i}^{n}) \tag{10}$$

Thermal Radiation Model

An energy balance on the ith node results in the following equation governing the net rate of energy absorbed at the ith node:

$$\dot{Q}_{\mathrm{abs}_i} = \dot{Q}_i + \dot{Q}_{R_i} - \dot{Q}_{\mathrm{ap}_i} - \dot{Q}_{\mathrm{shell}_i} \tag{11}$$

where for $i = 1, 2, \ldots, M$, the rate of energy reradiated from the jth node to the ith node and the rate of energy reradiated from the ith node back out through the aperture are, respectively,

$$\dot{Q}_{R_i} = \frac{A_i}{N} \sigma \sum_{j=1}^{M+1} f_{i-j}(T_j^4 - T_i^4) \tag{12}$$

$$\dot{Q}_{\mathrm{ap}_i} = \frac{A_i}{N} \sigma f_{i-\mathrm{ap}}(T_i^4 - T_{\mathrm{ap}}^4) \tag{13}$$

and the receiver shell loss per node is given by

$$\dot{Q}_{\mathrm{shell}_i} = \kappa(T_{\mathrm{av}})/NM \tag{14}$$

In this equation, the shell loss function $\kappa(T_{av})$ is recommended by Ensworth et al.[17] to be

$$\kappa(T_{av}) = b(T_{av}/T_{ref})^4 \tag{15}$$

where $b = 0.82$, $T_{ref} = 1860$ R (1033 K), and T_{av} is the instantaneous, spatially averaged canister outer surface temperature given by

$$T_{av}(t) = \frac{1}{L_{cav}} \int_0^{L_{cav}} T_1(z, t)\, dz \tag{16}$$

In addition, the geometric view factors shown in Eqs. (12) and (13) are given by analytic expressions found in Howell.[18]

Modified HOTTube Code

The numerical results presented in the present paper were generated using a modified version of the computer code HOTTube, which is a transient, time-explicit, axisymmetric total receiver thermal analysis code. HOTTube was initially developed by the AlliedSignal Aerospace Company for the Space Station *Freedom* solar heat receiver. The PCM melting and freezing processes are modeled using an enthalpy formulation with mushy zone prediction capability. Therefore, explicit interface tracking is not performed. The use of adiabatic spacers between canisters permit thermal decoupling axially in the containment tube and PCM but with two-dimensional thermal conduction in the working fluid conduit. As a result, a continuous interface along the axial direction does not develop. In addition, a one-dimensional, semianalytic thermal energy transport model is used for the working fluid coolant, which is justified by the small hydraulic diameter of 0.045 in. (0.1143 cm) for the annular flow region. Temperature-dependent thermophysical properties are taken into account for the working fluid coolant, containment canisters, and working fluid tube. Finally, an ideal-body thermal radiation model is assumed for the reradiative energy transport to and from the containment canister outer surface and receiver backwall. In addition, radiation losses through the aperture as well as conduction losses through the receiver shell are taken into account.

The physical domain is discretized into a 24 (axial) × 15 (radial) grid scheme and a time step of 60 ms is used, which is below that required for numerical stability. These are used after achieving grid independence. The receiver backwall is modeled using a single node (isothermal but time varying), as are the aperture and aperture plate. Because the incident flux distribution is considered the same for all tubes in the receiver, the radiative flux model includes the backwall, 24 axial rings, and the aperture and aperture plate, each of which are isothermal but time varying.

After all of the geometric view factors are calculated, reradiative energies from ring-to-ring, ring-to-backwall, ring-to-aperture plate, and vice versa, are evaluated. Finally, the net absorbed energy per node is calculated, which is the difference between the energy incident upon that node, energy reradiated from other nodes including the backwall and aperture plate, and energy lost from the node because of infrared emission back out through the aperture. This net-absorbed energy is used to drive the heat transfer and, ultimately, the phase-change process.

Convective effects caused by buoyancy, thermocapillarity, solutocapillarity, or volume change (void formation) are not included in the present model. This is partially justified by the use of adiabatic spacers, which will lead to substantially reduced hydrostatic potential in each canister because the liquid formed in each canister will be confined and not allowed to interact (neither thermally nor hydrodynamically) with liquid formed in the other canisters.

The numerical results from HOTTube, which were generated on Howard University's IBM ES 9000 mainframe computer, required approximately 20 CPU minutes per cycle.

Results and Discussion

The results presented in this section pertain to a maximum insolation orbit for the orbital altitude corresponding to 93 min total orbit time with 27 min of eclipse. This maximum insolation of approximately 1.26 suns (1 sun = 1.37 kW/m^2) is incidentally, the maximum output capability of the solar simulator lamps of the GTD system. The corresponding rate of energy crossing the aperture plane of the solar receiver during the simulated sun period is approximately 12.6 kW.

The nominal operating speed of the GTD engine's turboalternator work-producing shaft is 56,000 rpm, which yields a working fluid mass flow rate of approximately 0.3541 lbm/s (161 g/s). A map of TAC speed vs mass flow rate is provided by Shaltens and Mason,[14] from which a linear curve fit performed by the present authors is given by

$$\dot{m} = 0.0629(28.59) + 5.2 \times 10^{-6}(2.36 \times 10^{-3})\omega$$
$$44{,}000 \leq \omega \leq 58{,}000$$

where ω is the TAC speed in rpm and $\dot{m}$ is the working fluid mass flow rate in lbm/s (g/s).

The representative results pertain to seven test-point conditions obtained during November 1996 for the so-called hybrid configuration of the GTD system. Test points (TPs) 3–5 represent operations to achieve balanced-orbit conditions and TPs 6–9 represent operations to achieve steady-state conditions. TPs 1 and 2, in which some technical problems were encountered, were obtained during October 1996.

Solar Receiver Energy Balance

An important consideration in the numerical prediction of the solar receiver's thermal performance is the instantaneous overall energy balance. This is done to account for every unit of energy crossing the aperture plane per unit time. Figure 4 is a plot of the solar receiver's energy budget up to TP 3 (first balanced-orbit) conditions. The profile for the rate of energy crossing the aperture plane (labeled $\dot{Q}_{in}$) resembles a square pulse function, which illustrates the switching nature of consecutive sun periods and eclipse periods. If the receiver is truly balanced, then the sum (labeled $\dot{Q}_{total}$) of the rate of energy extracted by the gas (labeled $\dot{Q}_{gas}$), rate of energy lost by reradiation through the aperture and rate of energy lost through the receiver shell (labeled $\dot{Q}_{loss}$), and rate of energy stored inside the receiver (labeled $\dot{Q}_{stor}$) should also follow this square pulse function. This is indeed the case, as shown in Fig. 4, with a maximum error of less than 3%. This small error is primarily a result of the receiver shell heat-loss approximation.

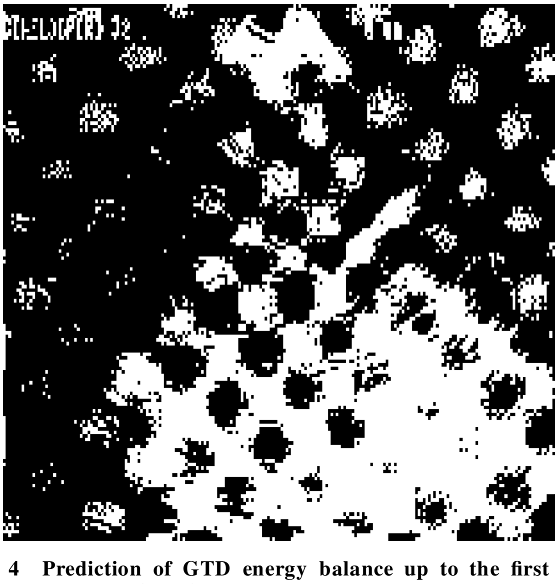

Fig. 4 Prediction of GTD energy balance up to the first balanced-orbit point (TP 3).

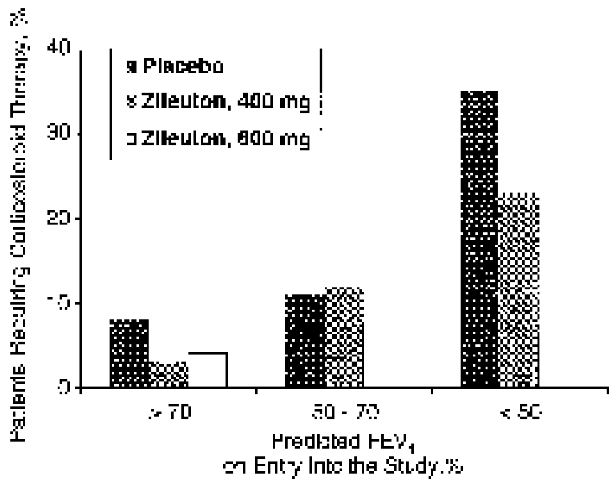

Fig. 5 Numerical prediction of GTD maximum canister surface temperature, average canister surface temperature, and receiver gas exit temperature over 21 orbit cycles, including the three indicated balanced-orbit (BO) points.

Temperature and Melt Fraction Predictions

Figure 5 shows the temporal progression of maximum canister outer surface temperature, average canister outer surface temperature, and receiver gas exit temperature from startup to 21 orbit cycles. The receiver heat input is fixed at 12.6 kW and the TAC speed varies from 0 at startup to 56,000 rpm (up to orbit 12) to 58,000 rpm (orbits 13–21). The transient operation for the orbital simulations is detailed as follows:

1) The startup mass flow rate is fixed at 0.005 lbm/s (2.3 g/s) until the maximum canister temperature reaches 1900°R (1056 K), after which it is increased to 0.3541 lbm/s (161 g/s) (this occurs during the second cycle); faster heat-up of the receiver is effected as a result.

2) Also during startup, the receiver gas exit temperature is fed back to the receiver inlet until the receiver inlet reaches 1508°R (838 K), which is accomplished during the first cycle; this is an expedient computational scheme that advances the numerical solution to the point where higher fidelity modeling can be initiated.

3) After the balanced-orbit for TP 3 is reached on orbit 6, the sun period is changed from 66 to 72 min for orbits 7–9; after the TP 4 balanced-orbit is reached on orbit 9, the sun period is further increased to 78, 81, and 84 min for orbits 10, 11, and 12, respectively; the receiver inlet temperature is increased to 1550°R (861 K), 1600°R (889 K), and 1550°R (861 K) for obits 10, 11, and 12, respectively; these changes are done to effect an increase in the amount of PCM in the liquid phase.

4) On orbits 13–21, the mass flow rate is increased to 0.3645 lbm/s (165 g/s); the receiver inlet temperature is sequentially decreased to 1525°R (847 K), 1475°R (819 K), 1450°R (806 K), and 1425°R (792 K) for orbits 13–16, respectively; the receiver inlet temperature remains fixed at 1425°R (792 K) for orbits 17–21; these changes are performed to effect increased removal of energy from the receiver.

For the numerical predictions, a balanced-orbit is declared when the difference between all calculated temperatures is less than 2°R (1.1 K) between successive sunrise and sunset conditions.

It is further observed from Fig. 5 that over most of the orbit cycles

$$T_{\max} > T_{\text{out}} > T_{\text{av}}$$

which is also observed in the experimental data (discussed in the next section). It is also observed that the maximum receiver exit temperature of 1958°R (1088 K), which is reached on the orbit 13 sunset, is within 0.2% of the experimental value of 1962°R (1090 K).

The corresponding fraction of receiver PCM in the liquid phase is illustrated in Fig. 6. Recall that the melting point of LiF-CaF–CaF$_2$ is 1873°R (1040 K) and its latent heat of fusion is 340 Btu/lbm (789 kJ/kg). For the GTD solar heat receiver, the total mass of PCM is 53 lbm (24 kg), which corresponds to a maximum latent storage capacity of 18,020 Btu (19 MJ or 5.3 kWh). It is observed that the maximum liquid fraction, which occurs on sunset for all representative cycles, reaches a maximum of 61% during the heat-up phase, 30% for TP 3, 36% for TP 4, a 56% local maximum on orbit 12, and 3% for TP 5, which is just out of the two-phase regime.

Comparison of Numerical and Experimental Results

To perform a direct comparison of modified HOTTube numerical predictions and GTD experimental results, the time scale for the experimental results had to be recalibrated to coincide with that used for the numerical predictions. This was done to mitigate any unmodeled dynamics associated with unexpected shutdowns and subsequent restarts, which occurred several times during the November 1996 test runs. As a result, comparisons are made from the first balanced-orbit (TP 3).

Figures 7 and 8 are comparisons of maximum and average canister outer surface temperatures, respectively, from TP 3 to

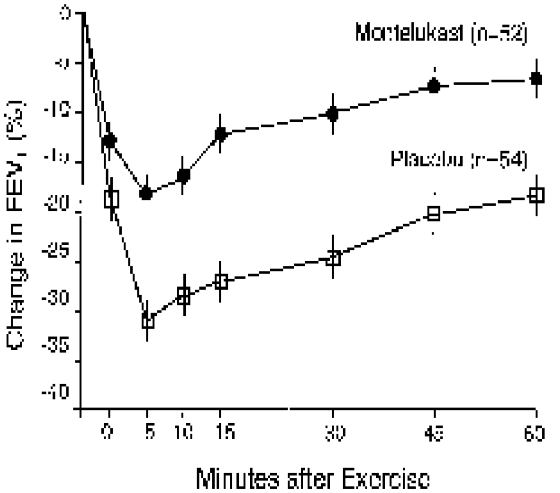

Fig. 6 Numerical prediction of the total fraction of PCM in the liquid phase over 21 orbit cycles.

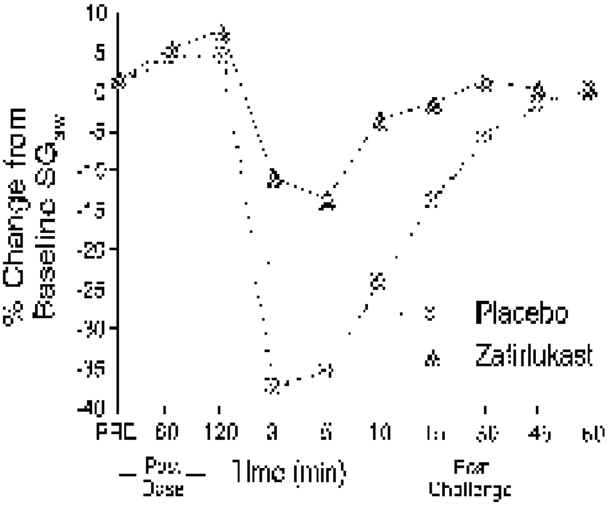

Fig. 7 Comparison of GTD numerical and experimental results for the maximum canister surface temperature starting from the first balanced-orbit point (TP 3).

orbit 21. The first thing to note is that there is good qualitative agreement with regard to temperature slopes during both orbital sun and eclipse periods. It is also observed that the ΔT between sunrise and eclipse is smaller for the numerical predictions during the first four cycles after TP 3, indicating increased melting over that which occurs in the experiment. There are several possible explanations of this behavior: 1) the effective thermal mass in the model is less than the actual receiver, which would tend to cause overpredictions; 2) uncertainties in the dynamics that occur before reaching TP 3 balanced-orbit conditions; and 3) differences in the receiver gas inlet profile. As the simulation progresses farther into the latent regime (between 5 and 8 orbits beyond TP 3), this ΔT is reduced, as expected. Finally, the remaining orbits beyond TP 3 indicate operation back into the subcooled regime, which is made possible by extended eclipse periods and higher TAC speed (mass flow rate). Another key observation is the significant difference (as high as 150°R or 83 K) between maximum and average canister temperatures. This is caused by the large variation in incident flux along the axis of the receiver tubes. However, in the latent regime, this difference is smaller, as expected.

A comparison of the receiver gas exit temperature is revealed in Fig. 9. Again, in comparison, the temperature slopes appear qualitatively similar throughout all orbit cycles beyond TP 3. However, larger differences between sunrise and sunset temperatures are observed, particularly in the latter orbits. This appears to be caused by apparent high sensitivity to changes in receiver inlet gas temperature. This sensitivity appears to diminish in the latent regime, as expected, because the heat transfer characteristics would approach that of a tube with isothermal boundary conditions. As a result, the receiver gas temperature would approach this isothermal condition asymptotically as the gas approached the receiver exit.

Tables 1 and 2 are comparisons of the solar heat receiver thermal performance for the steady-state test points (TPs 6–9). It should be noted that TPs 6–8 are in the sensible regime and TP 9 is in the latent regime. These comparisons are shown at reduced power levels (receiver heat input) and reduced TAC speeds (mass flow rates) as compared with TPs 3–5. A steady-state test point is declared when all temperature transients are within less than 5°R/h (2.8 K/hr). As shown in Tables 1 and 2, quantitative agreement is very good for all TPs represented. The maximum difference in receiver gas exit temperature, which occurs for TP 6, is 4°R (2.2 K), which results in a maximum error (over all TPs) of less than 0.3%. Similarly, the maximum error in receiver gas heat input, which occurs for TP 9, is less than 6%. Finally, the maximum error in receiver losses, which occurs for TP 6, is less than 11%. Also observe that while the HOTTube numerical results underpredict the

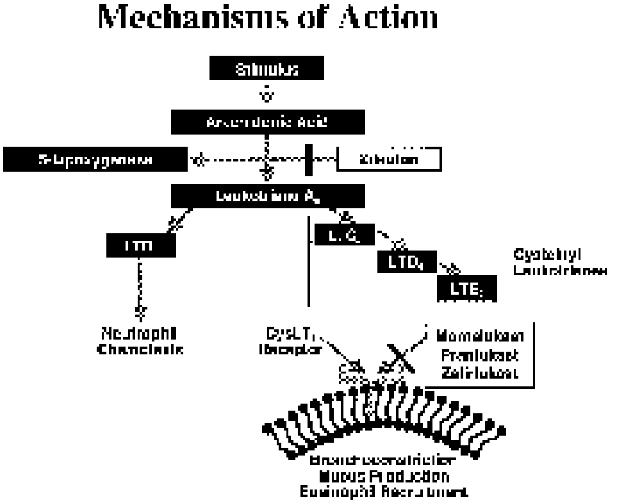

Fig. 8 Comparison of GTD numerical and experimental results for the average canister surface temperature starting from the first balanced-orbit point (TP 3).

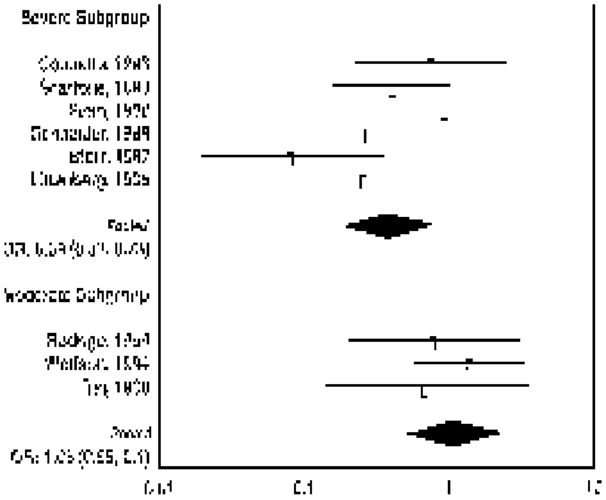

Fig. 9 Comparison of GTD numerical and experimental results for the receiver gas exit temperature starting from the first balanced-orbit point (TP 3).

Table 1 Comparison of steady-state test point performance of the GTD hybrid system configuration for TPs 6 and 7

System parameter	GTD experiment	TP 6	HOTTube	GTD experiment	TP 7	HOTTube
Receiver heat input, kW	—	7.01	——	——	6.79	——
TAC speed, rpm	——	52,000	——	——	48,000	——
Gas exit temperature, °R (K)	1661 (923)	——	1665 (925)	1735 (964)	——	1733 (963)
Gas heat input, kW	5.78	——	5.60	5.32	——	5.13
Receiver losses, kW	1.23	——	1.36	1.47	——	1.57

Table 2 Comparison of steady-state test point performance of the GTD hybrid system configuration for TPs 8 and 9

System parameter	GTD experiment	TP 8	HOTTube	GTD experiment	TP 9	HOTTube
Reciver heat input, kW	——	8.17	——	——	9.36	——
TAC speed, rpm	——	52,000	——	——	52,000	——
Gas exit temperature, °R (K)	1795 (997)	——	1794 (996)	1934 (1074)	——	1932 (1073)
Gas heat input, kW	6.50	——	6.21	7.10	——	6.68
Receiver losses, kW	1.67	——	1.81	2.26	——	2.40

receiver gas exit temperature (except TP 6) and gas heat input, the receiver losses are overpredicted.

Conclusions

A physical and numerical model of the solar heat receiver component of NASA Lewis Research Center's SD GTD system has been developed. Numerical and experimental results are compared for balanced-orbit and steady-state modes, and in both subcooled and latent (two-phase) regimes. Results show that while maximum and average canister outer-surface temperatures are relatively insensitive to changes in receiver gas inlet temperatures, receiver gas exit temperatures are very sensitive to changes in receiver gas inlet temperatures, particularly for operation in the subcooled regime. HOTTube predictions also show very good agreement with GTD experimental data for subcooled and latent steady-state modes.

Acknowledgment

The financial support to Howard University from the NASA Lewis Research Center under Grant NAG3-1907 is gratefully acknowledged.

References

[1] Strumpf, H., and Coombs, M. G., "Solar Receiver Experiment for the Hybrid Space Station Brayton Engine," *Proceedings of the ASME Solar Energy Division Conference* (San Diego, CA), American Society of Mechanical Engineers, New York, 1988.

[2] Sedgwick, L. M., "Solar Dynamic Heat Receiver Technology Design Analysis Report," The Boeing Co., Boeing Rept., D180-29711-1, Seattle, WA, Sept. 1988.

[3] Wichner, R. P., Solomon, A. D., Drake, J. B., and Williams, P. T., "Thermal Analysis of Heat Storage Canisters for a Solar Dynamic Space Power System," Oak Ridge National Lab., TM-10665, Oak Ridge, TN, April 1988.

[4] Wilson, D. G., and Flanery, R. E., "Modeling Cyclic Melting and Freezing in a Hollow Metal Canister," Oak Ridge National Lab., TM-6497, Oak Ridge, TN, Sept. 1988.

[5] Kerslake, T. W., and Ibrahim, M. B., "Two-Dimensional Model of a Space Station *Freedom* Thermal Energy Storage Canister," *Proceedings of the 25th Intersociety Energy Conversion Engineering Conference (IECEC)* (Reno, NV), 1990; also NASA TM 103124, Aug. 1990.

[6] Drake, J. B., "Modeling Convective Marangoni Flows with Void Movement in the Presence of Solid-Liquid Phase Change," Oak Ridge National Lab., TM-6516, Oak Ridge, TN, Jan. 1990.

[7] Hirt, C. W., and Nichols, B. D., "Volume of Fluid (VOF) Method for the Dynamics of Free Boundaries," *Journal of Computational Physics,* Vol. 39, No. 1, 1981, pp. 201–225.

[8] Kerslake, T. W., "Experiments with Phase Change Thermal Energy Storage Canisters for Space Station Freedom," *Proceedings of the 26th Intersociety Energy Conversion Engineering Conference (IECEC)*, Boston, MA, 1991; also NASA TM 104427, Aug. 1991.

[9] Strumpf, H., Avanessian, V., and Ghafourian, R., "Design Analysis and Life Prediction for the Brayton Engine Solar Receiver for the Space Station *Freedom* Solar Dynamic Option," *Proceedings of the 26th Intersociety Energy Conversion Engineering Conference (IECEC)*, Boston, MA, 1991, pp. 241–247.

[10] Strumpf, H., Avanessian, V., and Ghafourian, R., "Design Analysis and Containment Canister Life Prediction for a Brayton Engine Solar Receiver for Space Station," *Journal of Solar Energy Engineering*, Vol. 116, No. 3, 1994, pp. 142–147.

[11] Sedgwick, L. M., "Advanced Development Receiver Thermal Vacuum Tests with Cold Wall," NASA CR 187092, June 1991.

[12] Skarda, J. R. L., "Thermal Modeling with Solid/Liquid Phase Change of the Thermal Energy Storage Experiment," NASA TM 103770, Nov. 1991.

[13] Namkoong, D., Jacqmin, D., and Szaniszlo, A., "Effect of Microgravity on Material Undergoing Melting and Freezing—The TES Experiment," *Proceedings of the AIAA 33rd Aerospace Sciences Meeting and Exhibit* (Reno, NV), AIAA, Reston, VA, 1995; also NASA TM 106845, Jan. 1995.

[14] Shaltens, R. K., and Mason, L. S., "Early Results from Solar Dynamic Space Power System Testing," *Journal of Propulsion and Power*, Vol. 12, No. 5, 1996, pp. 852–858.

[15] Jeffries, K. S. (ed.), "Solar Dynamic Power System Development for Space Station *Freedom*," NASA RP 1310, July 1993.

[16] Hall, C. A., III, "Thermal State-of-Charge of Solar Heat Receivers for Space Solar Dynamic Power," Ph.D. Dissertation, Howard Univ., Washington, DC.

[17] Ensworth, C., McKissock, D., and Mason, L., "Comparison of CCEP with GTD Test Data," NASA Lewis Research Center, Internal Memorandum, Update #3, Aug. 1996.

[18] Howell, J. R., *A Catalog of Radiation Configuration Factors*, McGraw–Hill, New York, 1982.